**Abstract** A spaser is a nanoplasmonic counterpart of a laser, with photons replaced by surface plasmon polaritons and a resonant cavity replaced by a metallic nanostructure supporting localized plasmonic modes. By combining analytical results and first-principle numerical simulations, we provide a comprehensive study of the ultrafast dynamics of a spaser. Due to its highly-nonlinear nature, the spaser is characterized by a large number of interacting degrees of freedom, which sustain a rich manifold of different phases we discover, describe and analyze here. In the regime of strong interaction, the system manifests an irreversible ergodic evolution towards the configuration where energy is equally shared among all the available degrees of freedom. Under this condition, the spaser generates ultrafast vortex-like lasing modes that are spinning on the femtosecond scale and whose direction of rotation is dictated by quantum noise. In this regime, the spaser acquires the character of a nanoparticle with an effective spin. This opens up a range of interesting possibilities for achieving unidirectional emission from a symmetric nanostructure, stimulating a broad range of applications for nanoplasmonic lasers as unidirectional couplers and random information sources.
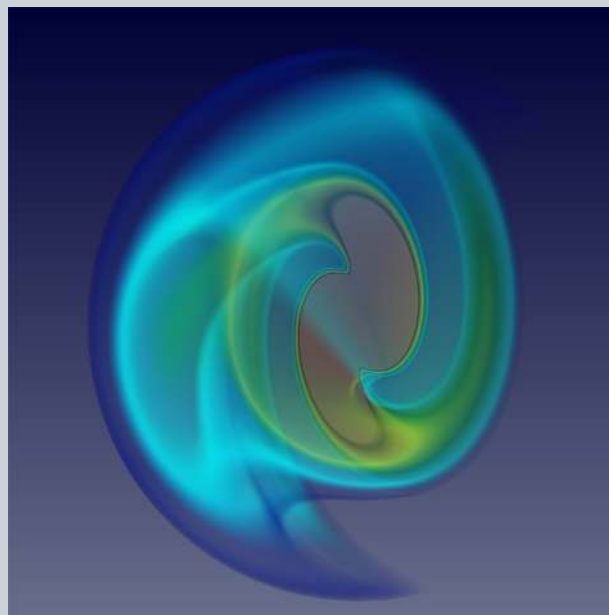
Energy equipartition and unidirectional emission in a spaser nanolaser

Juan Sebastian Totero Gongora[1],**Andrey E. Miroshnichenko**[2],**Yuri S. Kivshar**[2],**Andrea Fratalocchi**[1,*]

1. Introduction

Integrating coherent light sources at the nanoscale with spasers is one of the most promising applications of plasmonics [1–5]. In a spaser, localized plasmon polaritons (LPPs) waves occurring at the metal-dielectric interface are amplified by an active medium [1, 6]. Under specific conditions, the gain of plasmonic modes can overcome the absorption losses occurring in the metal and stimulated emission of radiation occurs, as experimentally observed in optically pumped spasers [5, 7–14]. Despite the large body of experimental research, the theoretical understanding of the spaser dynamics is still challenging. Fundamental insights on the lasing threshold conditions have been obtained by Mie theoretical approaches [15, 16] and semi-classical methods [17–22].

One of the most widely adopted configurations for the spaser is represented by a spherically symmetric nanostructure composed by a metallic core coated with a shell of resonant material [8]. Even for such a simple geometrical configuration, both the spatial distribution of the lasing modes and their temporal evolution are still unclear in many aspects.

While the core nanostructure supports strongly directional dipole modes [23], in fact, the symmetry of the system is expected to favor a rotational invariant laser emission. Understanding the competition between these opposite aspects, while furnishing new insights on the core-shell spaser, can provide key elements to govern the dynamics of energy emission from these structures.

Controlling the directionality of light in nanophotonic channels is a fundamental challenge in plasmonics, and is at the center of large research efforts [24–27]. The classical approach to address this issue is to use passive structures with broken symmetries, which scatter light in one preferential direction. An intriguing question is related to the possibility of achieving unidirectional emission from a perfectly spherical nanoparticle. Intuitively, one may expect that this would not be possible, due to the geometrical symmetry of the structure. However, we here illustrate that this counterintuitive dynamics is indeed feasible, thanks to the fundamental principle of energy equipartition. By leveraging on this thermodynamic principle, we illustrate how it is possible to observe very unconventional light-matter interactions in

---

[1] PRIMALIGHT, King Abdullah University of Science and Technology (KAUST),Thuwal 23955-6900, Saudi Arabia   [2] Nonlinear Physics Centre, Australian National University, Canberra ACT 2601, Australia.
[*] Corresponding author: e-mail: andrea.fratalocchi@kaust.edu.sa

spherically symmetric systems, enabling a new manifold of functionalities at the nanoscale with spaser technology.

2. Methods: numerical solution of Maxwell-Bloch equations with realistic quantum noise

A major experimental challenge in understanding the spaser lies in the difficulty of studying the lasing emission of a single nanostructure of $\approx 10 - 100$ nm size. In order to tackle this issue, we performed a series of massively parallel simulations where the first-principle equations of motions were solved without any approximation. Our approach combined dispersive Finite-Difference-Time-Domain (FDTD) for the evolution of the electromagnetic field and a fully quantum mechanical description of the gain medium through Bloch equations. The global set of equations is described as follows:

$$\begin{cases} \dfrac{\partial \mathbf{H}}{\partial t} = -\dfrac{1}{\mu_0} \nabla \times \mathbf{E}, \\ \dfrac{\partial \mathbf{E}}{\partial t} = \dfrac{1}{\varepsilon_0} \left[\nabla \times \mathbf{H} - \dfrac{\partial}{\partial t}(\mathbf{P}_{lin} + \mathbf{P}_{nlin}) \right], \end{cases} \quad (1)$$

where ε_0 is the electric permittivity, μ_0 the magnetic permeability and $\mathbf{E}$, $\mathbf{H}$ are electric and magnetic fields, respectively. In Equations (1), the polarization response of the material $\mathbf{P} = \mathbf{P}_{lin} + \mathbf{P}_{Nlin}$ is decomposed into linear $\mathbf{P}_{lin}$ and nonlinear $\mathbf{P}_{Nlin}$ contributions. The linear response is modeled by a general non-instantaneous term $\mathbf{P}_{lin}(t) = \varepsilon_0 \int dt' \chi(t - t') \mathbf{E}(t')$, which keeps into account the dispersive properties of the materials. The nonlinear polarization term $\mathbf{P}_{Nlin}$, conversely, describes the interaction between the electromagnetic field and the atoms composing the resonant medium.

In our model, we represented the active material by a quantum-mechanical four-level system, with three degenerate levels independently coupled to each component of the electric field. The dynamics of the atomic transitions are described by the following set of Bloch equations, which have been originally derived in [28, 29] and reported here for completeness:

$$\begin{cases} \mathbf{P}_{Nlin} = eq_0 N_a \left[S_1 \hat{\mathbf{x}} + S_4 \hat{\mathbf{y}} + S_9 \hat{\mathbf{z}} \right], \\ \partial_t S_l = \sum \Gamma_{lm} S_m - \dfrac{1}{\tau_l} \left[S_l - S_l^{(0)} \right], \\ \Gamma_{lm} = \dfrac{j}{2\hbar} \mathrm{Tr}\{ \mathscr{H}[\lambda_l, \lambda_m] \} \end{cases} \quad (2)$$

In Eqs. (2), e is the electric charge, q_0 is the quantum displacement length, N_a is the density of polarizable atoms in the excited state, τ_j are the atomic decaying constant rates and S_j represents the $j-$th component of the Bloch coherence vector $\mathbf{S}$, which combines different complex elements of the density matrix into a real vector state of the system. Expressions for the Hamiltonian $\mathscr{H}$ and the coupling components Γ_{lm} are found in [28, 30]. In Eqs. (2) the density of

excited atoms N_a plays the role of an external pumping rate, whose value is determined, as in a standard laser, by the external excitation. We explicitly considered the presence of quantum noise (further details can be found on the online Supporting Information) [31].

The Maxwell-Bloch approach described by Eqs. (1)-(2) has demonstrated to provide excellent quantitative predictions on a variety of nanolasers, including very complex geometries [32, 33]. All dispersive materials were modeled by employing a representation based on 4 Lorentz poles, which correctly represents the media response at visible wavelengths [35]. The quantum mechanical properties of Rhodamine were defined by the following set of parameters [29]:

$$\begin{cases} \omega_0 = 4.33 \cdot 10^{15} \text{ rad/s}, & q_0 = 0.1 \text{ nm}, \\ \tau_0 = 1 \text{ ps}, & \tau_1 = 10 \text{ fs}. \end{cases} \quad (3)$$

where ω_0 represents the emission frequency of the dye, τ_0 and τ_1 are the slow and fast relaxation rate of the atoms, respectively. In accordance with standard considerations on nanolasers with characteristic size much smaller than the wavelength [8] and with models based on full wave Maxwell-Bloch equations [29, 36], the system was assumed to be in an inverted population condition due the complete saturation of the dye molecules upon external illumination. We solved Eqs. (1) and (2) using our massively parallel FDTD simulator NANOCPP [30, 40, 52]. In our 2D and 3D simulations, the computational domain was organized as follows: the spaser was placed in the center of a box with 1 μm side, and each spatial direction was discretized with 400 points (spatial resolution in air: 2.5 nm). In order to simulate an open system, we used Uniaxial Perfectly Matched Layer (UPML) boundary conditions [53]. The computational part of this work is based on an extensive campaign of a few thousands of FDTD Maxwell-Bloch simulations, which have been performed on 8192 cores of our Shaheen II supercomputer cluster for a total simulation time of 25 millions cpu hours.

3. Results and discussion

3.1. An ab-initio *experiment: emergence of different phases in the spaser action*

We begin our analysis by considering a two dimensional core-shell spaser structure [10–14] composed by an Ag nanorod of radius $r = 8$ nm, embedded in a 32 nm thick silica shell doped with a Rhodamine dye amplifier. The advantages of this configuration are twofold: i) it opens to various experimental realizations with nanorods structures, whose fabrication can be fully controlled and ii) the results can be directly compared with experiments on single spasers, which to date are available only for 2D geometries [13, 14, 16, 20, 34]. The results of this analysis are then generalized to three-dimensional core-shell spasers by a set of 3D simulations.

Figure 1 summarizes our results for a TM polarized field

characterized by $E_x(x,z;t)$, $E_z(x,z;t)$ and $H_y(x,z;t)$ electromagnetic components. This was realized in the FDTD Maxwell-Bloch approach by enabling E_x and E_z transitions in the energy levels (see, e.g. [36] for more details). The system was excited with an angular frequency ω close to the resonant frequency ω_0 of the amplifying material. Due to the typical length of our simulations (tens of ps), we considered a continuous excitation. In our simulations, we monitored the spatio-temporal dynamics of the electromagnetic energy for a large temporal window ($t = 80$ ps) and for different values of the atomic density N_a, studying the formation of different lasing regimes in the spaser.

At low atomic densities $N_a < 10^{26}$ part/m^3, the system does not manifest lasing action, and is characterized by random fluctuations of the electromagnetic field (not shown in figure for simplicity). When $N_a = 2.25 \cdot 10^{27}$ part/m^3 (see Fig. 1a,d), the system exhibits an initial non-equilibrium regime characterized by the emission of pulses. After a transient, the spaser dynamics approaches a stationary emission pattern at $\omega = \omega_0$, which resembles an electric quadrupole (see Fig. 1a). If the atomic density is increased to $N_a = 3.75 \cdot 10^{27}$ part/m^3 (Fig. 1c,f) an even more interesting dynamics appears, where the spaser becomes a spinning dipole that rotates at the ultrafast frequency $v_0 = 689$ THz. The spinning direction of the spaser emission changes randomly from simulation to simulation, with a probability that is estimated to be 50%. The energy emission in the spinning phase is almost 10 times higher than in the multipole configuration. The spinning regime is attained after an intermediate phase (see Fig. 1b,e), where the energy dynamics shows a non-equilibrium configuration characterized by the alternation of both rotation and pulsation effects (see Fig. 1b).

3.2. Spaser as a complex nonlinear system

The lasing regimes displayed in Fig. 1 are the result of a complex form of light-matter interaction, which can be modeled by considering all the interacting degrees of freedom in the spaser. To study this problem, we developed a theoretical analysis whose dynamical variables can be extracted from first-principle simulations, allowing to validate our theory against realistic results. Following the angular spectrum representation approach [37], we decomposed the total emitted field as a superposition of modulated angular plane waves:

$$\mathbf{E}(\mathbf{x},t) = \hat{\mathbf{e}} \int_0^{2\pi} d\alpha \left[a_\alpha(t) \psi_\alpha(\mathbf{x}) e^{i\omega_0 t} + \text{c.c.} \right], \quad (4)$$

where $\omega_0 = ck$ is the field frequency, $\hat{\mathbf{e}}$ a dimensionless unit vector along the direction of $\mathbf{E}$, $a_\alpha(t)$ a generic mode amplitude and ψ_α is an outgoing plane wave that propagates on the angular direction defined by $\hat{\mathbf{s}} = [s_x, s_z] = [\cos\alpha, \sin\alpha]$:

$$\psi_\alpha(\mathbf{x}) = \exp\left[-ik \left(x\cos\alpha + |z|\sin\alpha \right) \right]. \quad (5)$$

Each term $a_\alpha = |a_\alpha| e^{i\theta_\alpha}$ can be considered as an angular spin variable, where the phase θ_α defines the orientation $\hat{\theta}_\alpha = [\cos\theta_\alpha, \sin\theta_\alpha]$, and $|a_\alpha|$ the amplitude. In our

analysis, stemming from the total field (4), we calculated the evolution of the spin variables in the far-field zone for $\alpha \in [0, 2\pi]$. This is accomplished by substituting Eqs. (4) into the Maxwell-Bloch Eqs. (1)-(2), and by applying perturbation analysis (see online Supporting Information for a detailed derivation):

$$\dot{\mathbf{A}} + \kappa\mathbf{A} = g\frac{\chi^{(1)} \cdot \mathbf{A}}{1 + \tau I} + \varepsilon g\tau \frac{\chi^{(3)} \vdots \mathbf{AAA}^*}{(1 + \tau I)^2} + O(\varepsilon^2), \quad (6)$$

where $\mathbf{A} = [a_0, ..., a_\alpha, ...]$ is a vector that contains the angular spin variables a_α, $\dot{\mathbf{A}} = d\mathbf{A}/dt$, $\tau = \tau_0/\tau_1$, $\varepsilon < 1$ a dimensionless perturbation constant, $I = \sum_\alpha |a_\alpha|^2$ the total intensity emitted by the laser, κ the material losses, g the active medium gain, $\chi^{(1)}$ and $\chi^{(3)}$ rank-2 and rank-4 tensors, respectively, behaving as first and third order susceptibilities of classical nonlinear optics [38]. In Eq. (6), all quantities are normalized to dimensionless units, and the relative expressions are detailed in the Supporting Information. Equation (6) shows that the spaser dynamics does not only depend on the competition between gain g and losses κ, but also from the relaxation times τ_0 and τ_1, which control the strength of high-order nonlinear interactions among the spins through the variable $\tau = \tau_0/\tau_1$. When the amplitude of $g\tau$ is small, high order nonlinear effects are suppressed and the system dynamics becomes expressed by a standard laser equation, with saturation effects provided by the term $1/(1 + \tau I)$. In this regime, the laser evolution can be easily discussed by moving to the space of the eigenstates b_β of the system, which is constructed from the eigenvectors φ_β and eigenvalues ξ_β of the linear susceptibility matrix $\chi^{(1)}$. Each eigenmode φ_β groups a set of angular spins a_α into a single eigenstate b_β, which evolves as follows (see Supporting Information):

$$\dot{b}_\beta + \kappa b_\beta = \frac{g\xi_\beta}{1 + \tau I} b_\beta, \quad (7)$$

with $I = \sum_\beta |b_\beta|^2$. The competition between gain and losses in this system has a very simple outcome, which always selects the eigenmode $\varphi_{\beta'}$ with the highest gain, reaching a steady state intensity $|b_{\beta'}|^2 = (g\xi_{\beta'} - \kappa)/\tau\kappa$. All the remaining eigenmodes with $\beta \neq \beta'$ are progressively suppressed at large times. This behavior relies on the fact that at steady-state, the intensity is constant $I = \sum_\beta |b_\beta|^2 = \text{const.}$ and Eq. (7) becomes a simple linear system with uncoupled states, which are all suppressed except the one with the largest gain. Figure 2a illustrates the evolution of Eqs. 7 in the case of $N = 30$ eigenstates, with eigenvalues ξ_β randomly distributed between zero and one. In the simulations we assumed $g = 1$, $\kappa = 0.1$ and $\tau = 10$. We considered an input condition where all the eigenstates are initially excited with the same amplitude and a random phase. In Fig. 2, we assigned a unique color to each eigenstate b_β, in order to identify the evolution of each state (Fig. 2, colorbar on the right).

When $g\tau$ is no longer negligible, Eq. (7) becomes:

$$\dot{b}_\beta + \kappa b_\beta = \frac{g\xi_\beta}{1+\tau I}b_\beta + \varepsilon g\tau \frac{\sum_{\eta,\nu,\rho}\xi^{(3)}_{\eta\nu\rho}b_\eta b_\nu b_\rho^*}{(1+\tau I)^2}, \quad (8)$$

where the tensor $\xi^{(3)}$ expresses the susceptibility $\chi^{(3)}$ in the space of eigenstates (see Supporting Information for more details on the transformation). In the dynamics encompassed by Eq. (8), all the states are now fully coupled. The dynamics of a single eigenstate, initially launched into the system, is no longer trivial. In the presence of many interacting states, the mode-competition resulting from (8) is expected to lead to a scenario of energy equipartition: at equilibrium, the system is expected to converge towards a configuration where each degree of freedom has the same amount of energy [39, 40].

In order to verify this hypothesis, we performed numerical simulations on (8) and considered 100 realizations of the dynamics of $N = 30$ modes, with $g = 1$, $\kappa = 0.1$, $\tau = 10$. The tensors ξ_n and $\xi^{(3)}$ where chosen as random matrices, with entries following a Gaussian probability density with unit mean value and unit variance. At the input, we launched a single mode β' with input intensity $I_0 = |b_{\beta'}(0)|^2$ that matches the steady-state intensity $I_0 = (g\xi_{\beta'} - \kappa)/\tau\kappa$. In the absence of nonlinear mode couplings, the excited mode maintains a constant intensity profile, showing practically no evolution from the initial state. In the presence of nonlinear coupling, however, the dynamics is quite different, as illustrated in Fig. 2b. In all cases examined, despite the fully random nature of the distribution of couplings furnished by $\xi^{(3)}$, the outcome observed is always the same: the system shows an irreversible evolution where the dynamics of the initial mode fades away, leading to the thermalization of energy among all the available states (Fig. 2b) and confirming our hypothesis of energy equipartition. The consequences of energy equipartition for a spaser are quite interesting, as we illustrate in the next section.

3.3. Phase diagram for a spaser

We calculated the emission dynamics of a spaser by extracting the time evolution of the spin variables a_α from FDTD simulations. By integrating Eq. (4) in the far field regime via the saddle-point method [41], one obtain the relationship between the angular spin variables a_α and the electric field:

$$\mathbf{E}_{r\to\infty}(s_x, s_z, t) = -i2\pi a_\alpha(t)\frac{e^{i(\omega_0 t - kr)}}{r}\hat{\mathbf{e}}, \quad (9)$$

with $r^2 = x^2 + z^2$. Equation (9) represents the intuitive idea that in the far-field, the electromagnetic field distribution can be modeled as an angular modulated wave, described by a cylindrical wave in 2D or a spherical wave in 3D. The angular spin variables a_α can be extracted from the amplitude of far-field component of the electric field $\mathbf{E}_{r=r_0\to\infty}(s_x, s_z, t)$ on a surface of constant radius $r = r_0$. To calculate the dynamic of a_α, we divided the angular domain $[0, 2\pi]$ into

$N = 100$ different angles α_j, and used a Near-to-Far-Field transformation (NTFF) to calculate the time evolution of the electric field $\mathbf{E}_{\alpha_j}$ along each angular direction α_j [53]. We then extracted the amplitude $|a_{\alpha_j}|$ and phase θ_{α_j} by employing a Hilbert transform on the time field evolution of the angular modes. To this extent, we first calculate the analytic representation $\mathbf{A}_{\alpha_j}$ of the electric field:

$$\mathbf{A}_{\alpha_j}(t) = \mathbf{E}_{\alpha_j} + i\mathscr{H}_l\{\mathbf{E}_{\alpha_j}\} \equiv \mathbf{X}_{c\alpha_j} + i\mathbf{X}_{s\alpha_j} \quad (10)$$

where $\mathscr{H}_l[f]$ indicates the Hilbert Transform on the generic field f. The amplitudes and phases are then expressed as follows:

$$|a_{\alpha_j}| = |\mathbf{X}_{c\alpha_j}|^2 + |\mathbf{X}_{s\alpha_j}|^2,$$

$$\theta_{\alpha_j} = \tan^{-1}\left(\frac{\mathbf{X}_{s\alpha_j}}{\mathbf{X}_{c\alpha_j}}\right). \quad (11)$$

In our simulations, we varied both the gain g and the strength of nonlinear interactions τ by acting on the atomic density N_a and the population relaxation time τ_0. We investigated a range of τ that covers typical dyes used in experiments [42] (Fig. 3a, solid lines). For each point in a (N_a, τ) phase-diagram, we calculated the far-field dynamics of the system and the evolution of the angular spins $a_\alpha(t)$, averaging over different realizations of quantum noise. The analysis shows that the spaser exhibits two different phases (Fig. 3a). When the parameter $N_a\tau$ is small, the system converges towards a dipolar emission of energy. Figure 3b illustrates the corresponding dynamics of the angular spin variables a_α, which redistribute the energy on a configuration corresponding to an electric quadrupole. This emission confirms the scenario predicted by our theoretical analysis for negligible nonlinear mode interactions: in this regime, in fact, the emission of energy occurs through the angular eigenstate that experiences the largest gain. In a spaser, angular eigenstates are electric dipolar modes, which are degenerate along all the possible orientations due to the rotational symmetry of the structure. Rotational symmetry is broken by the input excitation, which favors electromagnetic transitions along the axis of the electric field components E_x and E_z [43]. This imposes a specific distribution of angular gains, which have maxima for the quadrupole state observed in our simulations.

When the factor $N_a\tau$ increases, conversely, nonlinear mode interactions become important. In this situation, the system explores the full space of states and manifests energy equipartition (Fig. 3a,c). At steady state (Fig. 3c), each degree of freedom $|a_\alpha|e^{i\theta_\alpha}$ acquires the same energy $|a_\alpha|^2 = a^2$. Due to the rotational symmetry of the spaser, energy equipartition is exploited in a configuration that guarantees a radial emission of energy (Fig. 3c, inset). This implies that all the possible angular directions $\theta \in [0, 2\pi]$ are explored in sequence with $\theta = \pm\alpha$. By substituting such configuration of angular spins into (9), we obtain:

$$\mathbf{E}(\mathbf{r}, t) = -i2\pi a\hat{\mathbf{e}}\frac{e^{i(\omega_0 t - kr)\pm i\alpha}}{r}, \quad (12)$$

which represents the far-field expression of a rotating dipole. The rotation direction of the dipole is fully random, and dictated by quantum noise with a probability of 50% to select

counter clock-wise and clock-wise rotations. From the phase diagram of Fig. 3a, we also observe that when the parameter τ increases, the interactions among the modes become dominant, and the lasing action always converges towards energy equipartition. It is important to observe that when the spaser approaches energy equipartition, the transient dynamics shows the typical patterns of non-equilibrium thermodynamics. This aspect is observed in Fig. 1b,c: both systems are converging towards energy equipartition, but the case illustrated in Fig. 1c is characterized by stronger nonlinear interactions and thermalizes energy at a faster rate with respect to the case of Fig. 1b.

Figure 4 provides further details on the spasing action of the system, by showing the spectral narrowing (Fig. 4a solid red markers) and the nonlinear emission intensity (Fig. 4a solid blue markers) of the spaser for an increasing gain density N_a. In our simulations, we considered a Rhodamine dye (Fig. 3 solid red line). The results of this analysis agree very well with experimental measures reported in [13, 14]. The spasing action is confirmed by the characteristic "S"-shaped behavior of the intensity peak versus density N_a, and by the exponential narrowing of the emission linewidth that approaches an almost constant value in the spasing regime. The final linewidth of the spaser is of the order of $1 - 2$ nm, which is in quantitative agreement with experimental results [13, 14]. Both dipolar and rotational dynamics are observed in the spasing regime, within an order of magnitude of increase of the gain density N_a. The similitude of Fig. 4 with Fig. 3b of [14], suggests the possibility that the spasing rotational dynamics can be observed within the pumping ranges of current experiments.

3.4. Spasers as nanoplasmonic launchers and random information sources

We completed our analysis by investigating some possible applications of the spasers in the regime where energy equipartition takes place. A thorough analysis of this problem goes beyond the scope of this paper, and will be reported in a future work. An important problem in plasmonics is to achieve unidirectional light coupling, where the traffic of Surface Plasmon Polariton (SPP) waves can be manipulated and controlled at the nanoscale [26]. The possibility to obtain a stable rotating emission from a spaser could allow to integrate unidirectional energy sources in spherically symmetric systems, which are quite attractive due to their fabrication maturity.

In order to build an unidirectional launcher with spasers, we took inspiration from the large literature on rotating dipole systems [44, 45]. We investigated two simple configurations, illustrated in Fig. 5a-b and in the supporting movies SM1-SM2. In the first geometry, the spaser is placed near a metallic plane, made of Ag, with the nanostructure center displaced by 50 nm, corresponding to 0.1 λ, with λ the emission wavelength of the spaser. In our simulations, we modeled a Rhodamine 800 dye, with decaying constant $\tau_0 = 5 \cdot 10^{-10}$, whose parameters were taken from [42]. Figure 5c illustrates a snapshot of the electromagnetic energy density (semitransparent surface) for the geometry of Fig. 5a. As seen in the figure, the light matter interaction between the spaser and the metal induces the generation of unidirectional surface plasmon polariton (SPP) waves, which propagate along the metal-dielectric interface according to the rotation direction of the energy emitted by the spaser. The supporting movie SM1 illustrates in detail the time evolution of the system dynamics. In the rotational emission phase, the spaser acquires the character of a nanoparticle with a random effective 'spin'. Positive and negative spin signs correspond to counter-clockwise and clockwise rotations, respectively. In this simple nanoplasmonic circuit, the effective spin sign controls the coupling direction of light along the planar metallic surface. Figure 5d and the supporting movie SM2 illustrate the energy distribution corresponding to a different configuration, where the spaser is sandwiched between two identical tapered metallic nanostructures. This particular geometry can generate antisymmetric states along z, whose energy propagates along x always in both positive and negative directions.

3.5. Towards a three-dimensional rotating spaser

In order to verify the occurrence of a spinning phase in a spherical spaser, we performed a series of fully 3D simulations on a core-shell structure corresponding to the geometry that is experimentally investigated in [8]. A full analysis of the 3D spaser with a complete phase diagram for different N_a and combinations of optical dyes will be presented in a future work. Figure 6 summarizes the results obtained for $N_a = 7 \times 10^{27}$ and a Rodhamine dye, showing the formation of a spinning phase for this configuration. In our simulations we considered a linearly polarized excitation along (x, z), which drives the spaser towards a rotational emission in the same plane. This result further confirms that the rotational phase of the system is a general signature of energy equipartition that occurs in both 2D and 3D spasing geometries.

4. Conclusions and outlook

We have investigated the ultrafast dynamics of the spaser by both analytic theory and first-principle numerical methods, providing fundamental insights into the nonlinear evolution of the system. We have illustrated how a core-shell spaser, despite its simple geometry, shows a remarkable complexity that is able to sustain a rich scenario of different phases. This opens the attractive perspective of using spasers as new unidirectional couplers and random information sources. Compared to standard random sources based on chaotic data sequences, spasers are based on a fully physical process —i.e., quantum noise— which possesses an ideal infinite entropy and allows to generate random numbers whose sequence is never repeated. This can open new interesting applications in data cryptography, by using quantum noise as a physical one-way function [46].

Designing nanoscale energy sources where the symmetry of

the emission can be controlled is a quite interesting opportunity in the field of photonic quantum simulators as well. A central point in this field is related to the physical size of the simulator, which ultimately defines the time window of the quantum dynamics probed by the system [32, 47, 48]. To date, state-of-the-art architectures employ micron-sized photonic structures. An interesting question is related to the use of spasers as energy launchers for new types of nanoscale simulators, which can largely enhance the capabilities of current systems due to the nanoscale nature of the spaser. This question can stimulate new work in the field of quantum computing.

An important question is related to the dynamics of ensemble of spasers, where the random spin orientation can give rise to further possibilities to mold the flow of light at the nanoscale. Although a deeper discussion on this point goes beyond the scope of this work, some important points can be highlighted. Systems with random spins inspired a vast number of studies, which demonstrated fascinating applications ranging from novel classes of error correcting codes [49], to new concepts in neurobiology and the modeling of brain functions [50, 51]. A fundamental point is to understand the nonlinear interactions between different spasers and how their effective spin can be suitably "engineered". Once this question is properly addressed, spasers can open pathways toward the realization of nanoplasmonic neural networks, which can generate a novel manifold of nano-optics applications.

Supporting Information

Additional Supporting Information may be found in the online version of this article at the publishers website.

References

[1] D. J. Bergman and M. I. Stockman, Phys. Rev. Lett. **90**(Jan), 027402–027405 (2003).

[2] C. Rupasinghe, I. D. Rukhlenko, and M. Premaratne, ACS Nano **8**(3), 2431–2438 (2014).

[3] R. M. Ma, S. Ota, Y. Li, S. Yang, and X. Zhang, Nat. Nanotechnol. **9**(8), 600–604 (2014).

[4] T. P. H. Sidiropoulos, R. Roder, S. Geburt, O. Hess, S. A. Maier, C. Ronning, and R. F. Oulton, Nat. Phys. **10**(09), 870–876 (2014).

[5] Q. Zhang, G. Li, X. Liu, F. Qian, Y. Li, T. C. Sum, C. M. Lieber, and Q. Xiong, Nat. Commun. **5**(09) (2014).

[6] M. I. Stockman, Journal of Optics **12**(2), 024004 (2010).

[7] N. I. Zheludev, S. L. Prosvirnin, N. Papasimakis, and V. A. Fedotov, Nat. Photon. **2**(6), 351–354 (2008).

[8] M. A. Noginov, G. Zhu, A. M. Belgrave, R. Bakker, V. M. Shalaev, E. E. Narimanov, S. Stout, E. Herz, T. Suteewong, and U. Wiesner, Nature **460**(7259), 1110–1112 (2009).

[9] W. Zhou, M. Dridi, J. Y. Suh, C. H. Kim, D. T. Co, M. R. Wasielewski, G. C. Schatz, and T. W. Odom, Nature Nanotechnology **8**(7), 506–511 (2013).

[10] L. Zhang, J. Zhou, H. Zhang, T. Jiang, and C. Lou, Optics Communications **338**, 313 – 321 (2015).

[11] S. Y. Liu, J. Li, F. Zhou, L. Gan, and Z. Y. Li, Opt. Lett. **36**(7), 1296–1298 (2011).

[12] X. Meng, A. V. Kildishev, K. Fujita, K. Tanaka, and V. M. Shalaev, Nano Letters **13**(9), 4106–4112 (2013).

[13] J. Ho, J. Tatebayashi, S. Sergent, C. F. Fong, S. Iwamoto, and Y. Arakawa, ACS Photonics **2**(1), 165–171 (2015).

[14] Y. J. Lu, J. Kim, H. Y. Chen, C. Wu, N. Dabidian, C. E. Sanders, C. Y. Wang, M. Y. Lu, B. H. Li, X. Qiu, W. H. Chang, L. J. Chen, G. Shvets, C. K. Shih, and S. Gwo, Science **337**(6093), 450–453 (2012).

[15] J. A. Gordon and R. W. Ziolkowski, Opt. Express **15**(5), 2622–2653 (2007).

[16] X. L. Zhong and Z. Y. Li, Phys. Rev. B **88**(Aug), 085101 (2013).

[17] A. Chipouline, S. Sugavanam, V. A. Fedotov, and A. E. Nikolaenko, J. Opt. **14**(11), 114005 (2012).

[18] A. Veltri and A. Aradian, Phys. Rev. B **85**(Mar), 115429 (2012).

[19] J. B. Khurgin and G. Sun, Nature Photonics **8**(6), 468–473 (2014).

[20] E. S. Andrianov, A. A. Pukhov, A. V. Dorofeenko, A. P. Vinogradov, and A. A. Lisyansky, Optics Express **23**(17), 21983 (2015).

[21] V. Pustovit, F. Capolino, and A. Aradian, J. Opt. Soc. Am. B **32**(2), 188–193 (2015).

[22] E. S. Andrianov, A. A. Pukhov, A. V. Dorofeenko, A. P. Vinogradov, and A. A. Lisyansky, Physical Review B **85**(3), 035405 (2012).

[23] W. Liu, A. E. Miroshnichenko, D. N. Neshev, and Y. S. Kivshar, ACS Nano **6**(6), 5489–5497 (2012).

[24] J. Petersen, J. Volz, and A. Rauschenbeutel, Science **346**, 67–71 (2014).

[25] P. Alonso-González, A. Y. Nikitin, F. Golmar, A. Centeno, A. Pesquera, S. Vélez, J. Chen, G. Navickaite, F. Koppens, A. Zurutuza, F. Casanova, L. E. Hueso, and R. Hillenbrand, Science **344**, 1369–1373 (2014).

[26] A. E. Miroshnichenko and Y. S. Kivshar, Science **340**(6130), 283–284 (2013).

[27] X. Meng, U. Guler, A. V. Kildishev, K. Fujita, K. Tanaka, and V. M. Shalaev, Sci. Rep. **3**(February) (2013).

[28] A. Fratalocchi, C. Conti, and G. Ruocco, Physical Review A **78**(1) (2008).

[29] C. Conti and A. Fratalocchi, Nat. Phys. **4**(10), 794–798 (2008).

[30] J. S. T. Gongora and A. Fratalocchi, in: Computational Chemistry Methodology in Structural Biology and Material Sciences (Apple Academic Press, Oakville, 2015), chap. Ab-Initio Techniques For Light Matter Interaction At The Nanoscale.

[31] J. Andreasen, H. Cao, A. Taflove, P. Kumar, and C. q. Cao, Phys. Rev. A **77**(Feb), 023810 (2008).

[32] A. Fratalocchi, Nat. Photon. **7**, 271–273 (2013).

[33] C. Conti, M. Leonetti, A. Fratalocchi, L. Angelani, and G. Ruocco, Physical Review Letters **101**(14) (2008).

[34] X. Meng, K. Fujita, S. Murai, T. Matoba, and K. Tanaka, Nano Lett. **11**, 1374–1378 (2011).

[35] A. Vial, T. Laroche, M. Dridi, and L. Le Cunff, Appl. Phys. A Mater. Sci. Process. **103**(3), 849–853 (2011).

[36] G. M. Slavcheva, J. M. Arnold, and R. W. Ziolkowski, IEEE J. Sel. Top. Quantum Electron. **10**(5), 1052–1062 (2004).

[37] L. Novotny and B. Hecht, Dipole emission near planar interfaces, in: Principles of Nano-Optics, , second edition (Cambridge University Press, 2012), Cambridge Books Online.

[38] G. Agrawal and P. Govind, Nonlinear Fiber Optics (Academic, London, 1995).

[39] G. Gallavotti, Statistical Mechanics: A Short Treatise (Springer, Berlin, 2010).

[40] C. Liu, A. Di Falco, D. Molinari, Y. Khan, B. S. Ooi, T. F. Krauss, and A. Fratalocchi, Nat. Photon. **7**(6), 474–479 (2013).

[41] L. Mandel and E. Wolf, Optical Coherence and Quantum Optics (Cambridge University Press, New York, 1995).

[42] P. Sperber, W. Spangler, B. Meier, and A. Penzkofer, Opt. Quant. Electron. **20**(5), 395–431 (1988).

[43] C. Green, G. B. Mindlin, E. J. D'Angelo, H. G. Solari, and J. R. Tredicce, Phys. Rev. Lett. **65**(Dec), 3124–3127 (1990).

[44] J. P. B. Mueller and F. Capasso, Phys. Rev. B **88**(Sep), 121410 (2013).

[45] F. J. Rodríguez-Fortuño, G. Marino, P. Ginzburg, D. O'Connor, A. Martínez, G. A. Wurtz, and A. V. Zayats, Science **340**(6130), 328–330 (2013).

[46] R. Pappu, B. Recht, J. Taylor, and N. Gershenfeld, Science **297**(5589), 2026–2030 (2002).

[47] A. Crespi, R. Osellame, R. Ramponi, V. Giovannetti, R. Fazio, L. Sansoni, F. De Nicola, F. Sciarrino, , and P. Mataloni, Nat. Photon. **7**, 322–328 (2013).

[48] A. Aspuru-Guzik and P. Walther, Nat. Phys. **8**, 285–291 (2012).

[49] N. Sourlas, Nature **339**, 693–695 (1989).

[50] R. F. Langston, J. A. Ainge, J. J. Couey, C. B. Canto, T. L. Bjerknes, M. P. Witter, E. I. Moser, and M. B. Moser, Science **328**(5985), 1576–1580 (2010).

[51] D. J. Amit, Modeling brain function (Cambridge University Press, New York, 1992).

[52] M. L. Coluccio, F. Gentile, G. Das, A. Nicastri, A. M. Perri, P. Candeloro, G. Perozziello, R. Proietti Zaccaria, J. S. T. Gongora, S. Alrasheed, A. Fratalocchi, T. Limongi, G. Cuda, and E. Di Fabrizio, Science Advances **1**(8) (2015).

[53] A. Taflove and S. C. Hagness, Computational electrodynamics : the finite-difference time-domain method, 3rd edition, Artech House antennas and propagation library (Artech House, Boston, 2005).
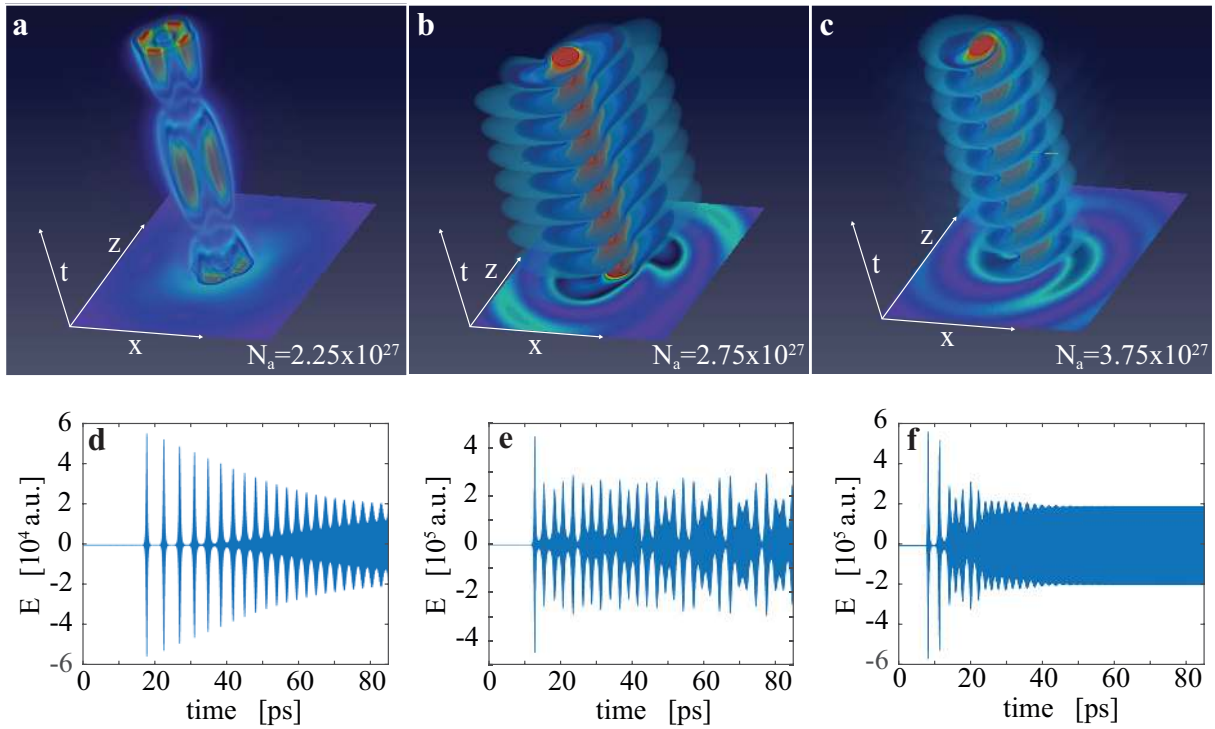
Figure 1 **First-principle results on the spaser emission under different dye doping concentrations** N_a. Panels (a)-(c) report the time evolution (vertical axis) of the (x, z) distribution of electromagnetic energy, which is illustrated with a semitransparent volume mapping. The total time window displayed in (a) is $2\pi/\omega_0 = 1.475$ fs, while in the panels (b-c) it has been increased to $8\pi/\omega_0 = 5.9$ fs to capture the rotational dynamics of the system. Panels (d)-(f) show the electric field evolution (normalized to a reference value E_0) probed in proximity of the spaser. Panels (a,d) correspond to the case of $N_a = 2.25 \cdot 10^{27}$ part/m^3, panels (b,e) to $N_a = 2.75 \cdot 10^{27}$ and panels (c,f) to $N_a = 3.75 \cdot 10^{27}$ part/m^3.
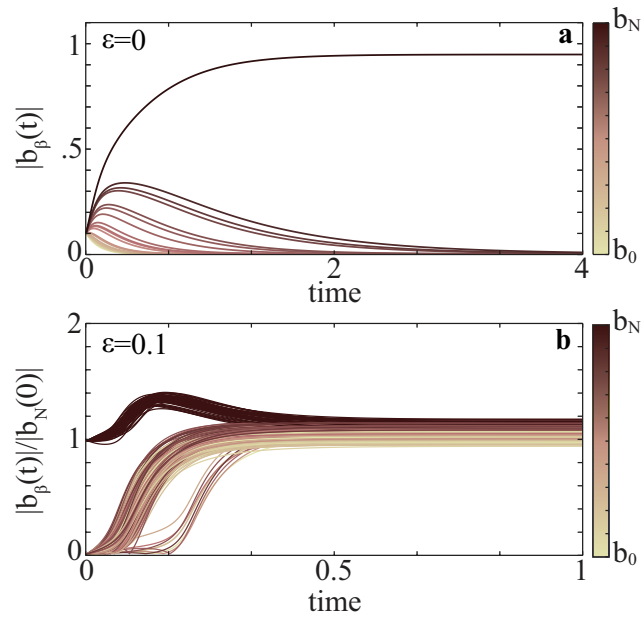
Figure 2 Study of energy equipartition in the spaser. Panel (a) shows the evolution of an ensemble of $N = 30$ eigenstates of the system in the case of $\varepsilon = 0$, when nonlinear interactions among the angular spins are absent. All eigenstates b_β are initially excited with the same amplitude and random phases. Each eigenstate has a gain coefficient equal to $g\xi_\beta$, with ξ_β uniformly distributed between 0 and 1, and is identified in the plot by a unique color (right colorbar). In the time dynamics, we observed that the eigenstate with the highest gain converges towards a nonzero stationary value, while all the others are progressively suppressed after an initial transient. Panel (b) analyzes the case for $\varepsilon \neq 0$, when nonlinear interactions affect the dynamics of the system. The panel illustrates the results of an ensemble of 100 different simulations, each considering the dynamics of a set of $N = 30$ eigenstates, with gain factors $\xi_\beta \in [0, 1]$ and fully random nonlinear couplings. In each simulation, we launched at the input the eigenstate with the highest gain, keeping all the other at zero amplitude. In this regime, the system shows always convergence towards energy equipartition. In all the simulations we used $g = 1$, $\kappa = 0.1$ and $\tau = 10$.
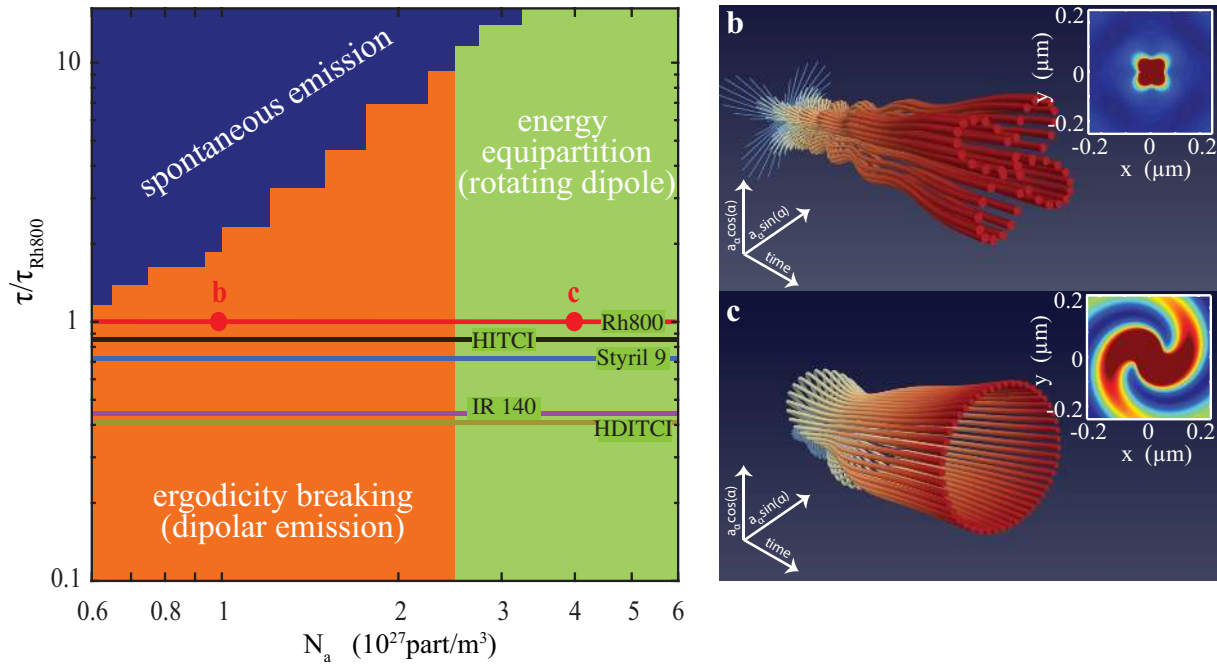
Figure 3 Phase diagram of the spaser and angular spin evolution. Panel (a) shows the phase diagram of the spaser in the $(g, \tau/\tau_{Rh800})$ plane, where we have scaled the parameter τ with respect to the corresponding value τ_{Rh800} of Rodhamine 800, a very common dye. Each phase is identified by extracting the dynamics of the angular spin variables a_α from the far-field of the system. The continuous lines in the plot indicates typical dyes available in the literature, with parameters taken from [42]. Panels (b) and (c) illustrate the dynamical evolution of the angular variables $a_\alpha(t)$, plotted in a three-dimensional space $(|a_\alpha| \sin \alpha, |a_\alpha| \cos \alpha, t)$, corresponding to the points b-c in the panel (a). The insets in panels (b) and (c) report a snapshot of the spatial distribution of the energy density emitted by the spaser at steady state.
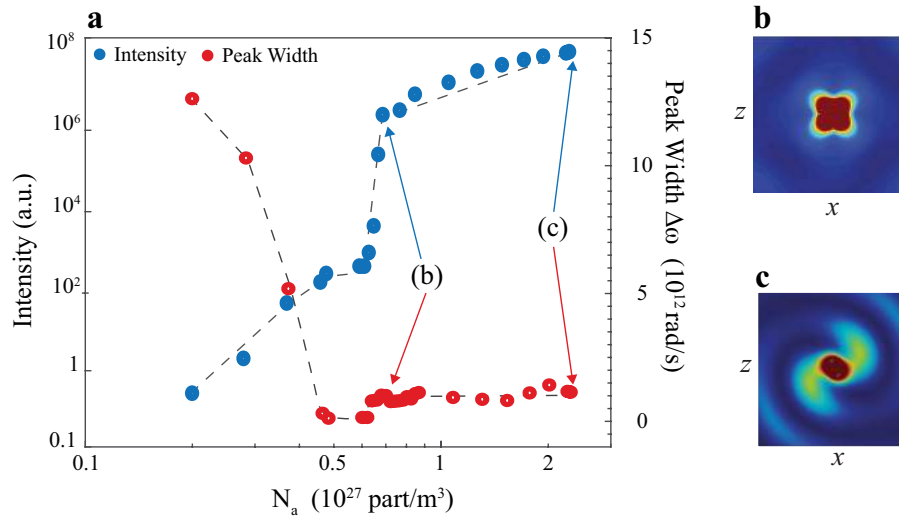
Figure 4 Lasing characterization and spasing threshold. Panel (a) Double logarithmic plot of lasing intensity (blue circles) and emission linewidth (red circles). Panel b and c show the spatial distribution of the emitted energy for two different gain densities, marked as points (b) and (c) in panel a. In the multipole lasing emission region (Panel a, point (b)), we observe the simultaneous occurrence of a nonlinear enhancement of the lasing intensity and the formation of a plateau in the spectral narrowing, which are the characteristic signature of a spasing transition. These results are in accordance with the experimentally observed transitions for single spaser structures [13, 14].
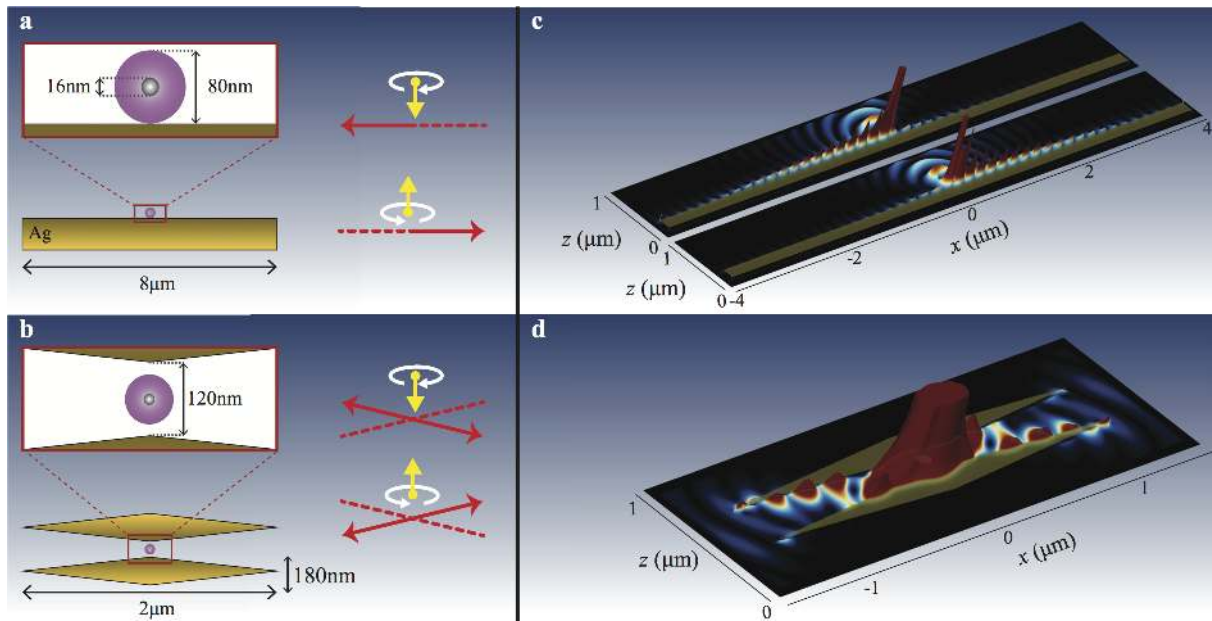
Figure 5 Analysis of different configurations of the spaser as unidirectional energy launcher and random energy source.
Panels (a-b) illustrate the setup of different configurations, with the working principle of the device summarized on the right. In panel (a), we considered a spaser placed in proximity of a metallic Ag surface (a, left). According to the spin orientation acquired by the laser in the rotational phase, energy is coupled on SPP wave trains that propagate in different directions along the x axis (a, right). In panel (b), conversely, we considered a tapered cross structure, where the spaser is placed in the center. This geometry always couples energy in both directions along x, but the states generated are always anti-symmetric along z. Panels (c-d) shows a snapshot of the energy distribution retrieved by FDTD simulations of the devices sketched in panels (a-b).
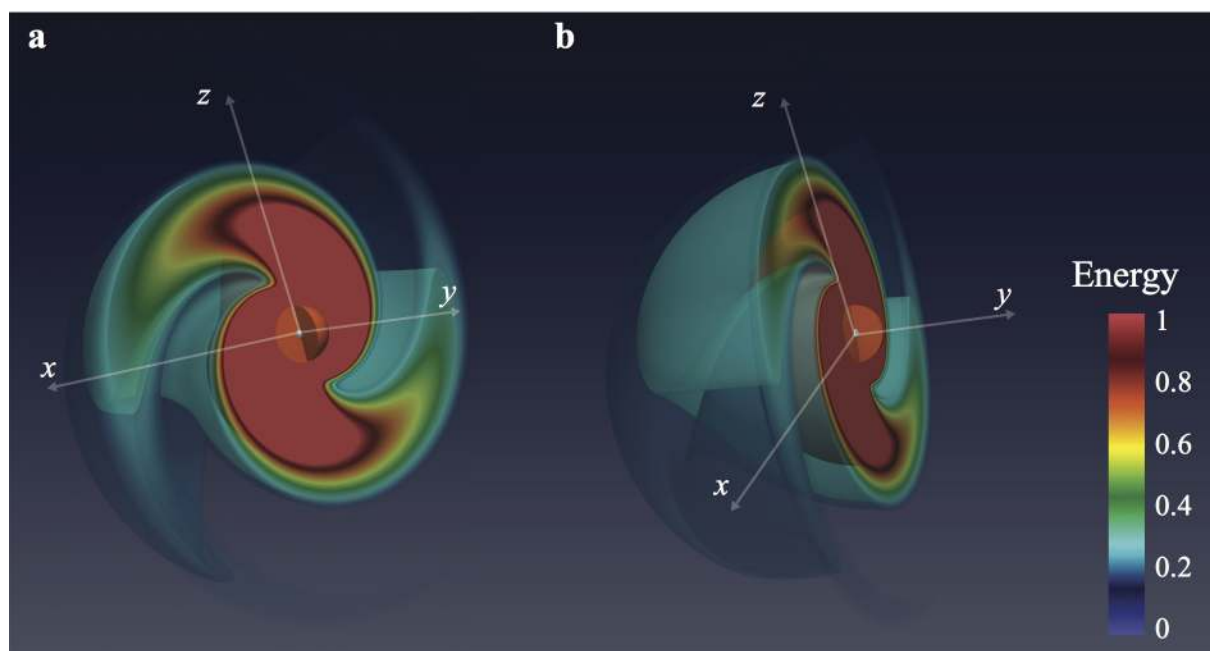
Figure 6 Rotational emission from a 3D spherical core-shell spaser. Panels a-b show two different perspective view of the electromagnetic energy distribution in the lasing stage at $t = 30$ ps for a fully three-dimensional spaser with $N_a = 7 \times 10^{27}$. A 3D section of the spaser nanoparticle is represented in the axis center. The incident polarization is linear along the (x, z) plane and the rotational emission occurs on the same plane.